Journal of
Materials Chemistry C

RSCPublishing

PAPER

View Article Online
View Journal | View Issue

Published on 30 July 2013. Downloaded by East China Normal University on 24/09/2013 00:13:18.

Cite this: *J. Mater. Chem. C*, 2013, **1**, 6252

Improved electric behaviors of the Pt/$Bi_{1-x}La_xFe_{0.92}Mn_{0.08}O_3$/$n^+$-Si heterostructure for nonvolatile ferroelectric random-access memory

Jinzhong Zhang, Zhihua Duan, Hao Zhang, Meijie Han, Yawei Li, Zhigao Hu* and Junhao Chu

Received 6th February 2013
Accepted 7th June 2013

DOI: 10.1039/c3tc30250d

www.rsc.org/MaterialsC

Multiferroic $BiFeO_3$ (BFO) and lanthanum-substituted $Bi_{1-x}La_xFe_{0.92}Mn_{0.08}O_3$ (BLFM*x*, $0 \leq x \leq 0.2$) films have been directly deposited on heavily doped Si(100) with an electric resistivity of about 0.001 Ω cm. The La substitution effects on the microstructure and lattice dynamics of the BLFM*x* films have been investigated by X-ray diffraction (XRD), scanning electron microscopy, far-infrared reflectance and Raman scattering studies. XRD analysis shows that the rhombohedral structure of BFO films reduced toward the orthorhombic or tetragonal structure by Mn and La substitution. It was found that the leakage current density tended to decrease with increasing La composition in a low electric field because the La dopant can suppress the formation of oxygen vacancies by stabilizing the oxygen octahedron and controlling the volatility of Bi atoms. On the other hand, the leakage current density in the high electric field can be suppressed by Mn substitution due to compensation of the charge of Fe^{2+} ions. The well-saturated polarization hysteresis can be obtained in the Pt/BLFM*x*/n^+-Si prototype devices. As an example, the electric remanent polarization ($2P_r$) and coercive field ($2E_c$) at the electric field of 1600 kV cm^{-1} for the BLFM0.15 film are 150 μC cm^{-2} and 870 kV cm^{-1}, respectively. Moreover, its relative dielectric constant at the frequency of 3.5×10^5 Hz is about 125. These results could be crucial for future applications of silicon-based nonvolatile ferroelectric random-access memory.

1 Introduction

Among multiferroic materials such as $BiFeO_3$ (BFO), $BiMnO_3$, $YMnO_3$, $TbMnO_3$ and $HoMnO_3$, BFO is known to be the only one with simultaneous ferroelectric ($T_c \approx 1103$ K) and G-type antiferromagnetic ($T_N \approx 643$ K) ordering at room temperature.[1–4] Generally, bismuth ferrite BFO has a rhombohedrally distorted perovskite ABO_3 structure, which belongs to the space group $R3c$ (C_{3v}^6) at ambient temperature and pressure. The primitive cell contains two formula units, which can be described by the displacement of Fe (Bi) cations along the pseudocubic [111] direction and an accompanying antiphase rotation of the neighboring FeO_6 octahedra.[5] At present, bulk BFO single crystals are not suitable for realization of miniaturization, integration and commercialization because of their high conductivity, high cost, and space-charge polarization dominated ferroelectric and dielectric response.[6] A BFO film has a large remanent polarization of about 100 μC cm^{-2} along the $[111]_c$ or $[001]_h$ direction of the pseudo-cubic or hexagonal structure in theory and experiments, as compared to its bulk counterpart.[7–9] Therefore, it can be used for nonvolatile ferroelectric random-access memory (NVFRAM), which has large capacity, ultra-fast operating speed (10^{-9} s), low-power consumption, and high ratio of resistance in forward and reverse directions.[10,11] However, there are some obstacles to be overcome in BFO films for NVFRAMs: high leakage current, ferroelectric reliability, high coercive field, the formation of the Schottky contact between metallic electrode and Si, *etc.*[12–15] Thus, many investigators have attempted to improve the electrical properties, especially the leakage current of BFO materials by selection of preparation conditions, substrates, buffer layer, substitution and so on.[9,11–17]

Generally, it is believed that the leakage current may arise from the microstructure, impure phase, formation of defects and chemical fluctuation, which are associated with oxygen vacancies (${V_o}^{2+}$) caused by the coexistence of Fe^{2+} ions and volatilization (↑) of Bi^{3+} ions in BFO films.[13,14,18] The main reaction mechanisms are $4Fe^{3+} + 2O^{2-} \Rightarrow 4Fe^{2+} + O_2\uparrow + 2{V_o}^{2+}$ and $2Bi^{3+} + 3O^{2-} \Rightarrow Bi_2O_3\uparrow + 2{V_{Bi}}^{3-} + 3{V_o}^{2+}$.[19] Based on the hypothesis of Spaldin, the ferroelectricity and magnetism of BFO material come mostly from the A site (Bi^{3+}) and B site (Fe^{3+}), respectively.[20,21] To be more accurate, the ferroelectricity is mainly attributed to the Bi $6s^2$ lone-pair electrons. They may hybridize with an empty p orbital and form a localized lobe, which causes a structural distortion.[22,23] Therefore, chemical modification of the Bi site for BFO is expected to improve the ferroelectric behavior. Among the doping

Key Laboratory of Polar Materials and Devices, Ministry of Education, Department of Electronic Engineering, East China Normal University, Shanghai 200241, China. E-mail: zghu@ee.ecnu.edu.cn; Fax: +86-21-54345119; Tel: +86-21-54345150

 This journal is © The Royal Society of Chemistry 2013

Published on 30 July 2013. Downloaded by East China Normal University on 24/09/2013 00:13:18.

elements, the rare earth elements, such as lanthanum (La), are adopted to enhance ferroelectric properties and decrease the leakage current because of the reduced oxygen vacancies by stabilizing the oxygen octahedron.[2,13,14,24] Moreover, it has been reported that the Mn^{3+} (d^5 configuration) substitution on the B site (Fe^{3+}, d^4 configuration) can increase the resistivity in the high electric field region due to the formation of more distorted (Fe, Mn)O_6 octahedra.[14,25] Thus, one can conclude that La and Mn codoping can improve ferroelectric and dielectric properties of the BFO system.

Although there are many reports about multiferroic BFO films on $CaRuO_3/(LaAlO_3)_{0.3}(Sr_2AlTaO_6)_{0.35}$, $SrRuO_3/SrTiO_3$, $LaNiO_3$/Si, indium tin oxide (ITO) as well as Pt(111)/Ti/SiO_2/Si substrates, it is rare to find those about the preparation and ferroelectric characterization of pure and chemically substituted BFO films deposited on heavily doped semiconductor substrates directly. The heavily doped silicon (Si) with an electric resistivity of about 0.001 Ω cm can be used as the bottom electrode of capacitors. As we know, the (La, Mn)-substitution can induce lattice distortion, reduce oxygen vacancies in the films, and form homogeneous microstructures. Moreover, the strategy of heavily doped Si adoption can avoid the charge injection at the ferroelectric–metal interface.[26] Note that the effects of chemical doping on the electrical properties of BFO have been widely reported.[11,15–17] Unfortunately, the electrical response of La and Mn doped BFO films prepared on heavily doped Si(100) substrates directly is still an open issue. Therefore, the ferroelectric behavior of (La, Mn)-substituted BFO films on n^+-Si substrates should be investigated systematically for the applications of spintronics, multiple-state memory, information storage process, uncooled-infrared detectors, *etc.*

In this article, pure BFO and $Bi_{1-x}La_xFe_{0.92}Mn_{0.08}O_3$ (BLFM*x*, $0 \leq x \leq 0.2$) films have been directly deposited on heavily arsenic (As)-doped Si(100) substrates by a modified sol–gel method. With increasing La composition, the morphology of the BLFM*x* films becomes more and more smooth and the leakage current density drastically decreases at the same electric field. The present investigation supplies another strategy to resolve the phenomenon of incompatibility between ferroelectrics and metal electrodes in integrated ferroelectric devices.

2 Experimental section

2.1 Synthesis of (Bi, La, Fe, and Mn)-precursors

The (Bi, La, Fe, and Mn)-precursors were prepared from citric acid ($C_6H_8O_7 \cdot H_2O$, 99.5%) based solution, using ethylene glycol monomethyl ether ($C_3H_8O_2$, 99.0%) as the solution and analytically pure bismuth nitrate pentahydrate [$Bi(NO_3)_3 \cdot 5H_2O$, 99.0%], lanthanum nitrate hexahydrate [$La(NO_3)_3 \cdot 6H_2O$, 98.0%], ferric nitrate nonahydrate [$Fe(NO_3)_3 \cdot 9H_2O$, 98.5%], and manganese acetate tetrahydrate [$Mn(C_2H_3O_2)_2 \cdot 4H_2O$, 99%] as the solutes. Note that an excess of 6 mol% Bi was added for the compensating Bi loss during the annealing process. The multiferroic BFO and $Bi_{1-x}La_xFe_{0.92}Mn_{0.08}O_3$ ($x = 0.00$, 0.05, 0.10, 0.15, and 0.20 or in short BLFM0.00, BLFM0.05, BLFM0.10, BLFM0.15, and BLFM0.20, respectively) films were deposited directly on heavily As-doped silicon (100) substrates (electrical resistivity ~0.001 Ω cm). A further increase in La composition will induce phase transitions from the rhombohedral *R*3*c* phase to a noncentric orthorhombic *C*222 one in the La concentration range of 0.2 to 0.6.[2,27] Finally, all of the 0.2 M (Bi, La, Fe, and Mn)-precursor solutions with different La compositions have been stirred for 12 h at about 50 °C to improve the homogeneity and stabilized for about 60 days to enhance the hydrolysis and polymerization.

2.2 Fabrication of BLFM*x* ($0 \leq x \leq 0.2$) films

The n^+-Si(100) substrates were cleaned in pure ethanol with an ultrasonic bath to remove physisorbed organic molecules from the surfaces. Then, the substrates were rinsed several times with deionized water. Finally, the wafers were dried in a pure nitrogen stream before the deposition of the films. The BFO and BLFM*x* films with different La compositions were deposited by spin coating of the 0.2 M solution onto the substrates at the speed of 3500 revolutions per minute for 20 s. The as-prepared layers were dried at 80 °C for 20 min, then prebaked at 200 °C for 10 min and 400 °C for another 10 min to remove residual organic compounds, followed by annealing at 600 °C for 5 min in a nitrogen atmosphere for crystallization. The coating and annealing-treatment procedures were repeated fourteen times to obtain the desired thickness.

2.3 Microstructure, morphology, and electrical characterization of BLFM*x* films

The crystalline structure of the BLFM*x* films was investigated by X-ray diffraction (XRD) using a Ni-filtered Cu Kα radiation source (D/MAX-2550V, Rigaku Co.). In the XRD measurement, a vertical goniometer (Model RINT2000) and continuous scanning mode (θ–2θ) were selected with a scanning rate of 10° min^{-1} and an interval of 0.02°. The surface morphology and thickness of the films were examined using a field emission scanning electron microscope (FESEM: Philips XL30FEG). The impact of La substitution on the lattice dynamics was characterized using a Bruker Vertex 80V Fourier transform infrared spectrometer with a DTGS detector and 6 μm thick mylar beamsplitter, and a micro-Raman spectrometer (Jobin-Yvon LabRAM HR 800 UV) with the 488 nm laser. Platinum (Pt) dots with the diameter of about 0.1 mm, deposited by the sputtering technique using a shadow mask and then heat treated, are used as top electrodes for electrical measurements. The leakage current was measured using an electrometer (Keithley 6517A). Finally, the ferroelectric behavior, dielectric behavior, and data retention of BLFM*x* films were recorded using a ferroelectric test system (Precision Premier II: Radiant Technologies Inc.), a dielectric analyzer (BDS40, Novocontrol Tech.), and a Radiant Technologies Precision Material Analyzer, respectively. Note that the data retention was recorded by using the pulse voltage of 40 eV and pulse width of 0.1 ms at room temperature.

3 Results and discussion

3.1 Microstructure analysis

The XRD patterns of the BFO and BLFM*x* films with different La compositions show that all the films are polycrystalline with a stronger (110) diffraction peak, the position (2θ) of which is

Published on 30 July 2013. Downloaded by East China Normal University on 24/09/2013 00:13:18.

located at about 32.3° (Fig. 1a). Besides the strong feature, there are several other weaker diffraction peaks (012), (202), (024), (122), (300), *etc.* and no impurity phase is observed, which confirms that the films are of a single perovskite phase with *R*3*c* symmetry (JCPDS card, no. 86-1518). It indicates that the Mn and La atoms have been successfully incorporated into the BLFM*x* host lattice. As shown in Fig. 1b, (104) and (110) diffraction reflections are clearly separated in the BFO film. Nevertheless, they are overlapped with a broadening peak when 10% Mn is substituted. This phenomenon suggests that the rhombohedral structure is distorted to a tetragonal or monoclinic one.[4] However, all the samples still show the rhombohedral structure without changing the original crystal structure. Note that the reflection peak marked by the symbol (*) is from Si (200) diffraction. Based on the (012) and (110) diffraction peaks, the lattice constant *a* (*b*) of La-doped BLFM*x* films decreases from 5.58 to 5.54 Å with the La composition since the radius of La^{3+} (1.16 Å) is smaller than that of Bi^{3+} (1.17 Å). However, the lattice constant *c* is slightly smaller than that of the BFO film (Table 1). The deviations of the lattice constants suggest that there are different lattice distortions in the BLFM*x* films. Moreover, based on the definition of the crystal lattice distortion rate ($\varepsilon = \beta/4 \tan \theta$), the broadenings and positions of the (110) diffraction peaks, the effects of La and Mn substitution on the crystal lattice distortion of BFO films can be evaluated to about 0.17%, 0.24%, 0.26%, 0.34%, and 0.47% for BLFM0.00, BLFM0.05, BLFM0.10, BLFM0.15, and BLFM0.20, respectively. Therefore, the lattice variation will affect the ferroelectric distortion, as discussed in the following.

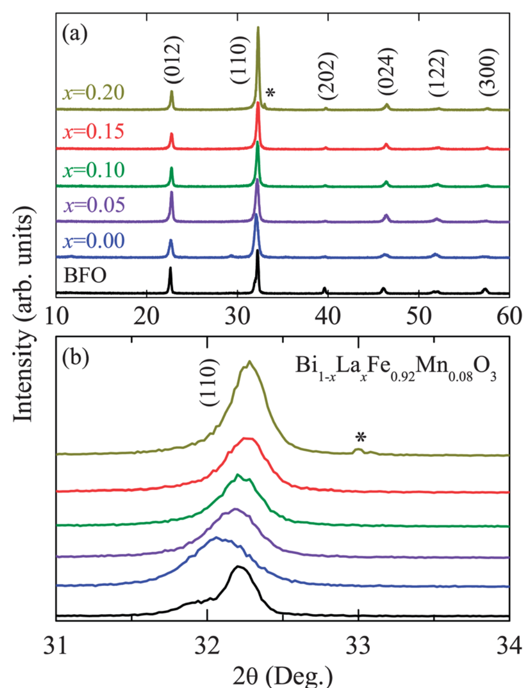

Fig. 1 (a) XRD patterns of BFO and BLFM*x* (*x* = 0.00, 0.05, 0.10, 0.15, and 0.20) films. (b) The enlarged (110) diffraction peak. The reflection peak marked by the symbol (*) originated from the Si substrate.

Table 1 The positions and FWHM of the (012) and (110) diffraction peaks for the BFO and BLFM*x* films determined from the XRD patterns

Samples	Peak positions (°)		FWHM (°)	Lattice constants	
(BLFM*x*)	(012)	(110)	(110)	*a* (*b*) (Å)	*c* (Å)
BFO	22.60	32.23	0.189	5.55	13.66
BLFM0.00	22.65	32.09	0.498	5.58	13.46
BLFM0.05	22.73	32.17	0.412	5.56	13.39
BLFM0.10	22.72	32.21	0.366	5.55	13.43
BLFM0.15	22.73	32.25	0.351	5.55	13.45
BLFM0.20	22.74	32.27	0.305	5.54	13.45

3.2 Lattice dynamics

Generally, multiferroic BFO material has a rhombohedrally distorted perovskite ABO_3 structure belonging to the space group *R*3*c* (C_{3v}^6) at ambient temperature and pressure. The primitive cell contains two formula units, which can be described by the displacement of Fe (Bi) cations along the pseudocubic [111] direction and an accompanying antiphase rotation of the neighboring FeO_6 octahedra.[5] According to the group theory, the zone-center optical phonon modes of the *R*3*c* phase are $4A_1 + 9E + 5A_2$.[28] The A_1 and doubly degenerate *E* modes are the first-order infrared- and Raman-active phonon modes, while the A_2 modes are silent ones.[29] Here, the phonon wave vector for the A_1 mode is along the *z* direction and the oscillator strength vectors for the E modes belong to the *x*–*y* plane.

Fig. 2a shows the four first-order infrared-active E modes predicted by group theory at room temperature, while others are strongly damped. It suggests that the *E*(TO2) and *E*(TO3) modes soften strongly, while the *E*(TO9) one hardens with the increasing La composition. Based on the calculated phonon frequencies, *E*(TO2) and *E*(TO9) are related to vibrations involving the Bi and O atoms, respectively. With increasing La

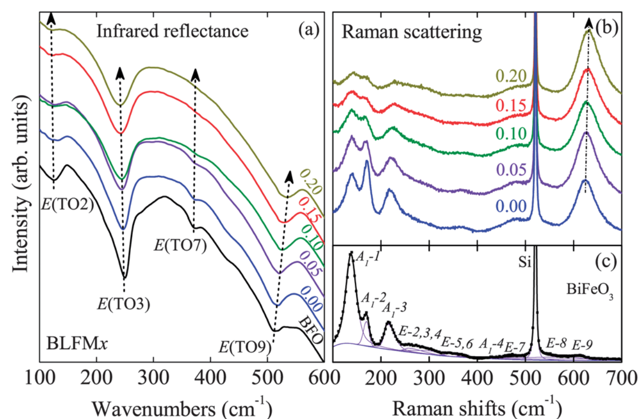

Fig. 2 (a) Infrared spectra of the BFO and BLFM*x* (*x* = 0.00, 0.05, 0.10, 0.15, and 0.20) films. The arrows show the variation trend of the infrared-active phonon frequencies at about 125, 245, 375, and 530 cm^{-1}. The infrared mode frequencies (b) Raman spectra of the BLFM*x*. The arrows show the variation trend of the phonon frequency at about 625 cm^{-1}. (c) The experimental (dotted line) and Lorentzian curve fitted (solid lines) Raman spectra of the BFO film.

This journal is © The Royal Society of Chemistry 2013

View Article Online

Published on 30 July 2013. Downloaded by East China Normal University on 24/09/2013 00:13:18.

composition, the E(TO2) and E(TO3) modes red shift by about 8 and 6 cm^{-1}, respectively. However, the E(TO7) located at about 375 cm^{-1} disappeared. On the other hand, the E(TO9) mode blue shifts by about 15 cm^{-1}. These behaviors indicate the decreasing rhombohedral elastic distortion, which can also be seen by increasing the temperature.[30]

Raman spectra of BLFMx and BFO films are shown in Fig. 2b and c, respectively. It suggests that incorporation of La and Mn into BFO makes significant changes in the peak intensity, broadening, and position. Theoretically, the Raman modes appeared in the low frequency region correspond to the Bi–O vibration. The broadenings of A_1 modes increase with increasing La composition which may be due to the La^{3+} substitution by Bi^{3+} and it is mainly attributed to the increasing dispersion in the Bi–O covalent bond length by rare earth La^{3+} ions.[25] In addition, the appearance of the strong peak located at about 625 cm^{-1} blue shifts by ~7 cm^{-1}, which originates from the stretching and bending of MnO_6 (Fe^{3+} substitution by Mn^{3+}) octahedra in the BLFMx films. Fig. 2b shows the illustration of the experimental (dotted line) and Lorentzian curve fitted (solid lines) Raman spectra of the pure BFO film. The first-order Raman-active modes observed from the spectra confirm rhombohedral symmetry and it is in accord with the XRD and infrared reflectance results.

3.3 Morphology

The typical SEM images show that pure BFO films have the biggest pores between the grains (Fig. 3). It suggests that there are many effects on the grain boundary and these effects could induce serious leakage. The Mn and La substitution significantly affects the morphologies and microstructure in the BLFMx films. The pores were reduced and the surface becomes smooth with the increasing La composition. In addition, the thickness of the films is about 270 ± 10 nm according to the cross-sectional SEM images. Moreover, transmission electron microscopy (TEM) shows that all the samples are well crystallized. The results of selected area electron diffraction (SAED) show that there are different lattice distortions in the BLFMx films, which are consistent with those of the XRD analysis. EDS spectra show that the as-prepared BLFMx samples consist of Bi, La, Fe, Mn, and O elements, and the atomic ratio of BLFMx samples approximates to the ideal stoichiometric values.

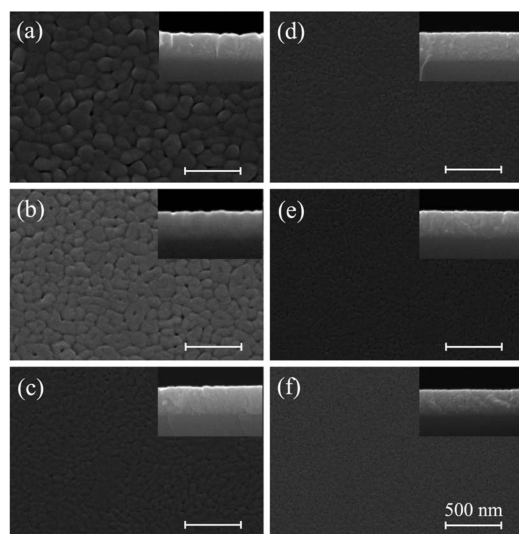

Fig. 3 The plane-view and the corresponding cross-sectional SEM images of (a) BFO, (b) BLFM0.00, (c) BLFM0.05, (d) BLFM0.10, (e) BLFM0.15, and (f) BLFM0.20 films on n^+-type Si(100) substrates.

3.4 Electrical properties

3.4.1 Interface layer effects between the film and the substrate. For the Pt/BLFMx/SiO_x/n^+-Si system, the existence of an oxide layer between the films and the Si substrates cannot be avoided during the annealing process. Therefore, the total capacitance C of the device is a series combination of the BLFMx film (C_f) and the oxide layer SiO_x (C_o) in a high frequency region: $1/C = 1/C_f + 1/C_o$. Here $C = \varepsilon_0\varepsilon_r S/d$, $\varepsilon_0 = 8.85 \times 10^{-12}$ F m^{-1}, ε_r is the relative dielectric constant and S is the area of electrodes.[31] Therefore, one can derive the expression: $\varepsilon_0 S/C = (1/\varepsilon_f)d_f + (1/\varepsilon_o)d_o$. In order to evaluate the thickness of the oxide layer, the BLFMx films with different La concentrations and thicknesses were fabricated by the same method and their dielectric responses have been investigated. Fig. 4a shows the $\varepsilon_0 S/C$ curves of the Pt/BLFM0.15/n^+-Si capacitors with different film thicknesses (d) of 95, 180, 250, and 345 nm. The thickness dependence of $\varepsilon_0 S/C$ can be well expressed by the linear relationships: $\varepsilon_0 S/C = 0.97(1) + 0.008d$ and $\varepsilon_0 S/C = 0.97(1) + 0.009d$ at the frequencies of 3.5 × 10^5 and 7.5 × 10^5 Hz, respectively (Fig. 4b). Therefore, the thickness of the oxide layer between the BLFMx films and n^+-Si substrates obtained was about 3.8 ± 0.1 nm based on the dielectric constant of SiO_2 ($\varepsilon_0 \approx 3.9$). Fig. 4c shows that the capacitor devices with higher La doping

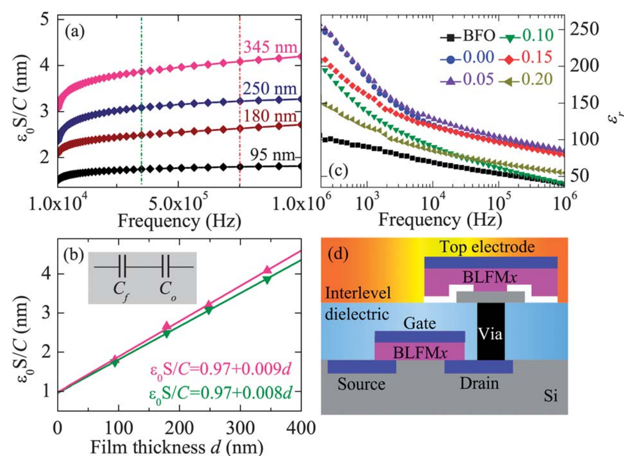

Fig. 4 (a) $\varepsilon_0 S/C$ curves of the BLFM0.15 films with thicknesses of 95, 180, 250, and 345 nm. (b) The experimental (dot lines) and linear fitting (solid lines) of the $\varepsilon_0 S/C$ as a function of film thickness d at frequencies of 3.5 × 10^5 and 7.5 × 10^5 Hz, which are shown by the dashed lines in (a). (c) Frequency dependence of the real part of dielectric constants (ε_r) of Pt/BLFMx/n^+-Si capacitors measured at room temperature. (d) Schematic diagram of the NVFRAM architecture, which contains one capacitor and one transistor to prevent crosstalk between adjacent cells, to probe the application of BLFMx films.

This journal is © The Royal Society of Chemistry 2013

Published on 30 July 2013. Downloaded by East China Normal University on 24/09/2013 00:13:18.

have higher dielectric constants. Considering lower leakage current, the sample BLFM0.15 is the best one in the present case. High dielectric constant ferroelectrics can be used as the gate insulator in metal-oxide-semiconductor field-effect transistors, as shown in Fig. 4d. Accurately, it illustrates the schematic diagram of the NVFRAM architecture, which contains one capacitor and one transistor to prevent crosstalk between adjacent cells.[10]

3.4.2 Leakage current mechanism of BLFM*x* films. Leakage current densities (J) of BFO and BLFM*x* film capacitors were recorded with both polarities of the applied electric field at room temperature (Fig. 5a). It indicates that the current density of the BFO films is the lowest in a lower electric field region, while it increases sharply in the high electric field region because of oxygen vacancies, Fe^{2+}, porous microstructure and grain boundary in the BFO film. As compared to the pure BFO film, the breakdown characteristic of the films is improved remarkably by Mn substitution in the high electric field region because the Mn substitution will reduce oxygen vacancies, stabilize perovskite, deform $(Fe, Mn)O_6$ octahedra, and increase the packing density.[25] Moreover, it was found that the leakage current density decreases slightly with the increasing La composition because the La dopant can suppress the formation of oxygen vacancies by stabilizing the oxygen octahedron, controlling volatility of Bi atoms and improving the packing density. Moreover, the leakage current density curves are not symmetric, which may be related to a possible asymmetry of electrode material interface-different work functions of top (Pt) and bottom electrodes (n^+-Si). To confirm the reason behind asymmetric leakage current density curves, we fabricated and characterized the Pt/BLFM*x*/Pt devices with the same electrode material (Pt). Their leakage current density curves are almost symmetric.

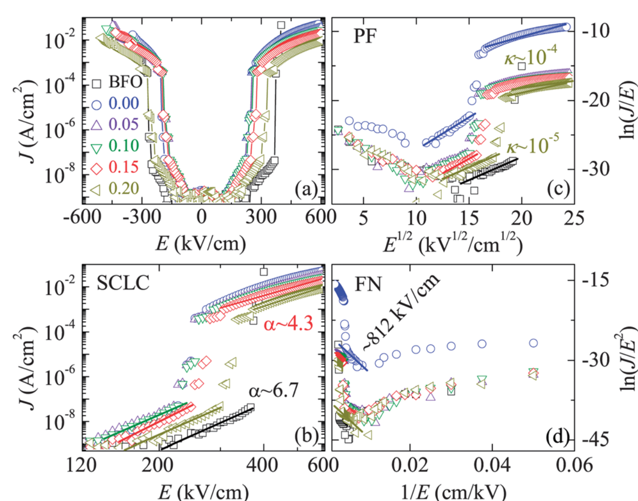

Fig. 5 (a) Log(J) − E, (b) log(J) − log(E), (c) ln(J/E) − $E^{1/2}$, and (d) ln(J/E^2) − 1/E of BFO and BLFM*x* films on n^+-Si substrates at room temperature. Note that different fits of these data are applied to determine the leakage mechanism of BFO and BLFM*x* (x = 0.00, 0.05, 0.10, 0.15, and 0.20) films. The parameters α and κ are the slope and optical dielectric constant, respectively.

In order to find out the leakage mechanism of BFO and BLFM*x* films, the conduction behavior of the films need a further study. The leakage current curves can be divided into several regions: Space-charge-limited conduction (SCLC), Poole–Frenkel emission, and Fowler–Nordheim tunneling.[32,33] In the low electric field region, SCLC is the dominating leakage process according to the well-known theory: $J_{SCLC} = 9\mu\varepsilon_0\varepsilon_r E^2/8d$, as shown in Fig. 5b. Here μ is the charge carrier mobility, ε_0 is the dielectric constant of free space, ε_r and d are the relative dielectric constant and thickness of films, respectively. It indicates that electrons are injected into the samples and the electron density becomes greater than that of thermally stimulated ones.[34] With increasing electric field, the current density increases because the defects in films trap free carriers, which are derived from electrodes. In addition, Fig. 5c shows the J/E as a function of $1/E^{1/2}$ based on the equation of the Poole–Frenkel emission (PF): $J_{PF} = CE\exp[-(E_I - q\sqrt{qE/(\pi\varepsilon_0 k)})/(k_B T)]$. Here C is a constant, E_I is the trap ionization energy, q is the electronic charge, k is the optical dielectric constant, and k_B is the Boltzmann constant. This mechanism arises from the field thermal ionization of trapped carriers into the conduction band of films.[35] It illustrates that the PF model can be ruled out from the plots in Fig. 5c. On the other hand, the interface-limited Fowler–Nordheim tunneling (FN) is considered to explain the leakage mechanism of the samples in the high electric field due to the narrowed oxide energy barrier width. It can be expressed as $J_{FN} = CE^2\exp[-D^2\sqrt{\varphi^3}/E]$, here $C = q^2/(8\pi h\varphi)$, $D = -8\pi\sqrt{2qm^*}/(3h)$, h is the Plank's constant, φ is the potential barrier height, and m^* is the effective mass.[36,37] Fig. 5d shows the illustration of the ln(J/E^2) plots of BFO and BLFM*x* films as a function of 1/E. It suggests that the FN model is considered as a possible current transport mechanism of BLFM*x* films in the high electric field region. Furthermore, the thickness and temperature dependence of J–E curves of the BLFM*x* devices has been investigated (not shown). It confirms that the SCLC theory is the dominating leakage process in the low electric field region, while the FN model is considered as a possible current transport mechanism in the high electric field region.

3.4.3 Ferroelectric properties of BLFM*x* films. The ferroelectric hysteresis loops of the Pt/BLFM*x*/n^+-Si capacitor were measured at room temperature and f = 2 kHz. For example, Fig. 6a and b show the P–E curves of Pt/BLFM0.05/n^+-Si and Pt/BLFM0.15/n^+-Si capacitors, respectively. With increasing La composition, the hysteresis loops of BLFM*x* films become better saturated, while the remanent polarization ($2P_r$) decreases (Fig. 6c). The hysteresis loops of the pure BFO film are not well shaped because of the large coercive field and leakage current in the high electric field region. The electric field in the films is as high as 1600 kV cm^{-1} and cannot increase for the applications of BLFM*x*, even though the data in Fig. 6a and b are not saturated. Moreover, pulsed polarization positive up-negative down (PUND) measurements are used to determine the switchable component since the P–E data may be inflated by leakage and need further clarification.[1,38] For example, the PUND data from the BLFM0.20 film are added in the inset of Fig. 6c. Generally,

This journal is © The Royal Society of Chemistry 2013

Published on 30 July 2013. Downloaded by East China Normal University on 24/09/2013 00:13:18.

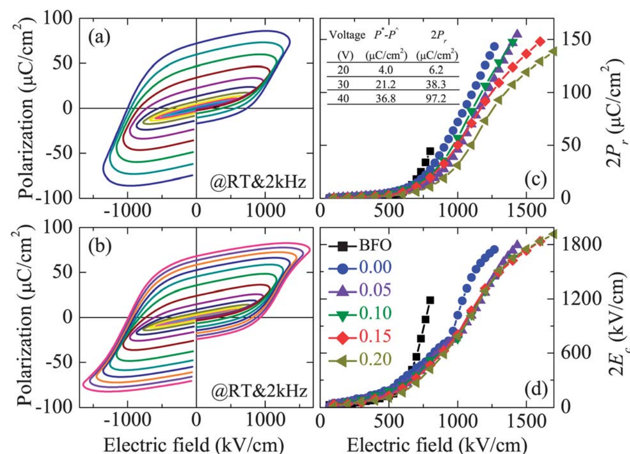

Fig. 6 Polarization-electric field (P–E) loops of (a) BLFM0.05 and (b) BLFM0.15 measured at 2 kHz. (c) $2P_r$ and (d) $2E_c$ of pure BFO and BLFMx films with different La compositions. The inset table shows the pulsed remanent polarization data from the BLFM0.20 film. Note that the parameters P* and P^ are the switched polarization and the nonswitched polarization, respectively.

the values of the pulsed remanent polarization are slightly smaller than those derived from P–E hysteresis loops. Although the values derived from two different techniques are unequal, they are nearly of the same magnitude. Moreover, as one of the most crucial parameters for memory, the retention tests have been carried out as shown in Fig. 7. After a retention time of about 10^5 s, the polarization loss was only about 2% for an applied electric field of about 1000 kV cm^{-1}. It indicates good retention characteristics and facilitates its application in ferroelectric memory.[39] It should be emphasized that the data retention was recorded at room temperature.

On the other hand, the variation trend for the PUND data is consistent with those from P–E hysteresis loops, which increases with the electric field. As we know, ferroelectric properties of BFO films are affected by various factors, such as oxygen vacancies, microstructure, lattice distortion, electrical instability of the Fe^{3+}, film thickness, substrates, *etc.* The results of XRD and SEM suggest that the La and Mn substitution can improve ferroelectric properties by inducing lattice distortion and forming homogeneous microstructures. Moreover, Fig. 6c

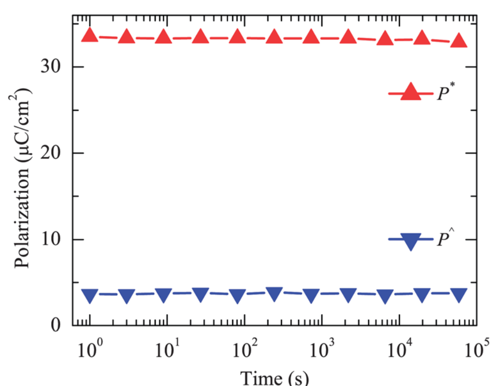

Fig. 7 Data retention curve characteristics of the BLFM0.15 films at room temperature.

and d show that the measured $2P_r$ and coercive field ($2E_c$) values at the electric field of about 1600 kV cm^{-1} for the Pt/BLFMx/n$^+$-Si capacitor are about 150 μC cm^{-2} and 1850 kV cm^{-1}, respectively. The $2P_r$ value is slightly larger than that (~110 μC cm^{-2}) of the BFO/$SrRuO_3$/$SrTiO_3$ samples prepared by pulsed laser deposition and about four times larger than that (~35 μC cm^{-2}) of $Bi_{0.9}La_{0.1}FeO_3$ ceramics.[1,13] The ferroelectric BLFMx layer maintains an induced polarization (a logic state "0" or "1") in the absence of a voltage. This physical feature provides a unique nonvolatility of ferroelectric capacitive memory. It should be pointed out that the coercive field values of BLFMx on n$^+$-Si substrates are much larger than that (~1000 kV cm^{-1}) of the ones on Pt/Ti/SiO_2/Si substrates prepared by the same method. This physical phenomenon may be due to the existence of an oxide layer between the BLFMx films and the Si substrates, which cannot be avoided during the annealing process. Based on the existence of the interface layer (SiO_x) between film and substrate, the $2E_c$ at the frequency of 2 kHz and electric field of 1600 kV cm^{-1} for the 270 nm thick BLFM0.15 film can be derived to be about 870 kV cm^{-1} and the other electric field of about 870 kV cm^{-1} located in the silicon oxide layer. Correspondingly, the relative dielectric constants of BLFM0.15 films at the frequencies of 3.5 × 10^5 and 7.5 × 10^5 Hz are about 125 and 110, respectively.

4 Conclusion

In summary, high-quality La-substituted BLFMx ($0 \leq x \leq 0.2$) films have been directly deposited on n$^+$-type Si (100) substrates by chemical solution deposition employing a spin-coating process. The XRD analysis shows that the films exhibit the pure perovskite phase structure. The rhombohedral structure is distorted to a tetragonal one by doping Mn and La elements. Moreover, the substitution of Mn and La suppresses the leakage current density and enhances the ferroelectric behavior by formation of homogeneous microstructures and inducing lattice distortion and so on. To put it concretely, (i) the La dopant can suppress the formation of oxygen vacancies by stabilizing the oxygen octahedron and controlling volatility of Bi atoms, and (ii) Mn substitution will compensate the charge of Fe^{2+} ions. In the low electric field region, SCLC is the dominating leakage process, while the FN model is considered as a dominant current transport mechanism in BLFMx films in the high electric field region. As an example, the remanent polarization P_r of 75 μC cm^{-2} and the coercive field E_c of 435 kV cm^{-1} at the electric field of 1600 kV cm^{-1} were achieved for a 270 nm thick BLFM0.15 film. The large coercive field may be ascribed to the existence of an oxide layer between the film and the substrate as well as the intrinsic properties of BFO. The present results could be crucial for future applications of silicon-based integrated circuits.

Acknowledgements

One of the authors (J.Z. Zhang) is grateful to Yude Shen, Xia Zhu, Yuanyuan Liao, and Xiao Chen for the technical support. This work was financially supported by the Major State Basic

Published on 30 July 2013. Downloaded by East China Normal University on 24/09/2013 00:13:18.

Research Development Program of China (Grant no. 2011CB922200 and 2013CB922300), the Natural Science Foundation of China (Grant no. 11074076, 60906046, and 61106122), the Project of Science and Technology Commission of Shanghai Municipality (Grant no. 11520701300), and the Program for Professor of Special Appointment (Eastern Scholar) at Shanghai Institutions of Higher Learning, and the project from East China Normal University (no. MXRZZ2012009).

Notes and references

1 J. Wang, J. B. Neaton, H. Zheng, V. Nagarajan, S. B. Ogale, B. Liu, D. Viehland, V. Vaithyanathan, D. G. Schlom, U. V. Waghmare, N. A. Spaldin, K. M. Rabe, M. Wuttig and R. Ramesh, *Science*, 2003, **299**, 1719–1722.
2 G. Catalan and J. F. Scott, *Adv. Mater.*, 2009, **21**, 2463–2485.
3 P. Rovillain, R. de Sousa, Y. Gallais, A. Sacuto, M. A. Méasson, D. Colson, A. Forget, M. Bibes, A. Barthélémy and M. Cazayous, *Nat. Mater.*, 2010, **9**, 975–979.
4 J.-H. Lee, M.-A. Oak, H. J. Choi, J. Y. Son and H. M. Jang, *J. Mater. Chem.*, 2012, **22**, 1667–1672.
5 P. Chen, X. Xu, C. Koenigsmann, A. C. Santulli, S. S. Wong and J. L. Musfeldt, *Nano Lett.*, 2010, **10**, 4526–4532.
6 K. Kalantari, I. Sterianou, S. Karimi, M. C. Ferrarelli, S. Miao, D. C. Sinclair and I. M. Reaney, *Adv. Funct. Mater.*, 2011, **21**, 3737–3743.
7 M. Ramazanoglu, M. Laver, W. Ratcliff II, S. M. Watson, W. C. Chen, A. Jackson, K. Kothapalli, S. Lee, S. W. Cheong and V. Kiryukhin, *Phys. Rev. Lett.*, 2011, **107**, 207206.
8 C. Ederer and N. A. Spaldin, *Phys. Rev. B: Condens. Matter Mater. Phys.*, 2005, **71**, 224103.
9 F. Yan, M.-O. Lai, L. Lu and T.-J. Zhu, *J. Phys. Chem. C*, 2010, **114**, 6994–6998.
10 O. Auciello, J. F. Scott and R. Ramesh, *Phys. Today*, 1998, **51**, 22–27.
11 A. Q. Jiang, C. Wang, K. J. Jin, X. B. Liu, J. F. Scott, C. S. Hwang, T. A. Tang, H. B. Lu and G. Z. Yang, *Adv. Mater.*, 2011, **23**, 1277–1281.
12 X. Wang, G. Hu, L. Cheng, C. Yang and W. Wu, *Appl. Phys. Lett.*, 2011, **99**, 262901.
13 S. Y. Wang, X. Qiu, J. Gao, Y. Feng, W. N. Su, J. X. Zheng, D. S. Yu and D. J. Li, *Appl. Phys. Lett.*, 2011, **98**, 152902.
14 H. Ishiwara, *Curr. Appl. Phys.*, 2012, **12**, 603–611.
15 A. Tsurumaki, H. Yamada and A. Sawa, *Adv. Funct. Mater.*, 2012, **22**, 1040–1047.
16 J. G. Wu and J. Wang, *Acta Mater.*, 2010, **58**, 1688–1697.
17 I. C. Infante, S. Lisenkov, B. Dupé, M. Bibes, S. Fusil, E. Jacquet, G. Geneste, S. Petit, A. Courtial, J. Juraszek, L. Bellaiche, A. Barthélémy and B. Dkhil, *Phys. Rev. Lett.*, 2010, **105**, 057601.
18 N. A. Spaldin, S.-W. Cheong and R. Ramesh, *Phys. Today*, 2010, **63**, 38–43.
19 J. G. Wu, J. Wang, D. Q. Xiao and J. G. Zhu, *J. Appl. Phys.*, 2011, **109**, 124118.
20 N. A. Hill, *J. Phys. Chem. B*, 2000, **104**, 6694–6709.
21 A. Filippetti and N. A. Hill, *Phys. Rev. B: Condens. Matter Mater. Phys.*, 2002, **65**, 195120.
22 C. H. Yang, J. Seidel, S. Y. Kim, P. B. Rossen, P. Yu, M. Gajek, Y. H. Chu, L. W. Martin, M. B. Holcomb, Q. He, P. Maksymovych, N. Balke, S. V. Kalinin, A. P. Baddorf, S. R. Basu, M. L. Scullin and R. Ramesh, *Nat. Mater.*, 2009, **8**, 485–493.
23 D. Kan, L. Pálová, V. Anbusathaiah, C. J. Cheng, S. Fujino, V. Nagarajan, K. M. Rabe and I. Takeuchi, *Adv. Funct. Mater.*, 2010, **20**, 1108–1115.
24 I. O. Troyanchuk, D. V. Karpinsky, M. V. Bushinsky, O. S. Mantytskaya, N. V. Tereshko and V. N. Shut, *J. Am. Ceram. Soc.*, 2011, **94**, 4502–4506.
25 C. M. Raghavan, D. Do, J. W. Kim, W.-J. Kim and S. S. Kim, *J. Am. Ceram. Soc.*, 2012, **95**, 1933–1938.
26 S. H. Baek, J. Park, D. M. Kim, V. A. Aksyuk, R. R. Das, S. D. Bu, D. A. Felker, J. Lettieri, V. Vaithyanathan, S. S. N. Bharadwaja, N. Bassiri-Gharb, Y. B. Chen, H. P. Sun, C. M. Folkman, H. W. Jang, D. J. Kreft, S. K. Streiffer, R. Ramesh, X. Q. Pan, S. Trolier-McKinstry, D. G. Schlom, M. S. Rzchowski, R. H. Blick and C. B. Eom, *Science*, 2011, **334**, 958–961.
27 A. Zalesskii, A. Frolov, T. Khimich and A. Bush, *Phys. Solid State*, 2003, **45**, 141–145.
28 J. Hlinka, J. Pokorny, S. Karimi and I. M. Reaney, *Phys. Rev. B: Condens. Matter Mater. Phys.*, 2011, **83**, 020101.
29 P. Hermet, M. Goffinet, J. Kreisel and P. Ghosez, *Phys. Rev. B: Condens. Matter Mater. Phys.*, 2007, **75**, 220102.
30 R. P. S. M. Lobo, R. L. Moreira, D. Lebeugle and D. Colson, *Phys. Rev. B: Condens. Matter Mater. Phys.*, 2007, **76**, 172105.
31 S. M. Sze and K. K. Ng, *Physics of Semiconductor Devices*, Wiley, New Jersey, 2007, Part II, ch. 4.
32 J. G. Wu, J. Wang, D. Q. Xiao and J. G. Zhu, *J. Mater. Chem.*, 2011, **21**, 7308–7313.
33 J. G. Wu, J. Wang, D. Q. Xiao and J. G. Zhu, *AIP Adv.*, 2011, **1**, 022138.
34 M. Kuik, G.-J. A. H. Wetzelaer, J. G. Laddé, H. T. Nicolai, J. Wildeman, J. Sweelssen and P. W. M. Blom, *Adv. Funct. Mater.*, 2011, **21**, 4502–4509.
35 J. G. Simmons, *Phys. Rev.*, 1967, **155**, 657–660.
36 M.-S. Wang, Q. Chen and L.-M. Peng, *Small*, 2008, **4**, 1907–1912.
37 A. A. Al-Tabbakh, M. A. More, D. S. Joag, I. S. Mulla and V. K. Pillai, *ACS Nano*, 2010, **4**, 5585–5590.
38 L. You, E. Liang, R. Guo, D. Wu, K. Yao, L. Chen and J. Wang, *Appl. Phys. Lett.*, 2010, **97**, 062910.
39 I. Stolichnov, A. K. Tagantsev, E. Colla, N. Setter and J. S. Cross, *J. Appl. Phys.*, 2005, **98**, 084106.

This journal is © The Royal Society of Chemistry 2013